Thermal behaviour assessment and electrical characterisation of a cylindrical Lithium-ion battery using infrared thermography

(Article begins on next page)

05 November 2024

Thermal behaviour assessment and electrical characterization of a cylindrical Lithium–ion battery using infrared thermography

Luca Giammichele [a,*], Valerio D'Alessandro [a] Matteo Falone [a], Renato Ricci [a]

[a] *Dipartimento di Ingegneria Industriale e Scienze Matematiche*
Università Politecnica delle Marche
Via Brecce Bianche 12, 60131 Ancona (AN), Italy

---

1 **Abstract**

2 This paper presents an experimental evaluation of the thermal and electrical per-
3 formance of a commercial 26650 cylindrical LiFePO$_4$ battery cell. The thermal
4 management of lithium–ion batteries is a key problem for electric mobility appli-
5 cations, where batteries are subjected to severe operating conditions. Accordingly,
6 this study aims to demonstrate the reliability of infrared thermography in the
7 quantitative analysis of heat generation in battery cells. In our opinion, infrared
8 thermography can be very attractive owing to: (i) the non-contact nature of this
9 technique and (ii) its capability to quickly scan measurement areas. Consequently,
10 infrared thermography and thermocouple probe results were compared, providing
11 evidence of similar behaviour. Moreover, we present an electrical characterisation of
12 our lithium–ion battery. In particular, the cell potential, open circuit potential, and
13 entropic heat coefficient vis–à–vis the state of charge were experimentally measured.
14 The obtained experimental data were used to evaluate a simplified heat generation
15 term that is widely employed in numerical approaches. The different contributions
16 to heat generation were carefully analysed. The results show that the reversible
17 term considerably influences the total thermal power. Moreover, infrared–based heat
18 generation estimation can be considered reliable.

19 *Key words:* IR thermography, Lithium–ion batteries, Thermal management,
20 Electrochemical heat generation

21

---

* Corresponding author.
 Email addresses: `l.giammichele@staff.univpm.it` (Luca Giammichele),
`v.dalessandro@univpm.it` (Valerio D'Alessandro), `m.falone@pm.univpm.it`
(Matteo Falone), `ricci@univpm.it` (Renato Ricci).

Nomenclature

Acronyms

$BTMS$ Battery Thermal Management System

$CCCV$ Constant Current Constant Voltage

EHC Entropic Heat Coefficient

EV Electric Vehicles

IR Infrared

SOC State of Charge

Subscript

e Environment

eod End of discharge

in Initial value

IR Infrared thermography

s Surface

tc Thermocouple

Symbols

$\dot{Q}$ Thermal power $[W]$

$\dot{Q}_{irr}$ Irreversible thermal power $[W]$

$\dot{Q}_{rev}$ Reversible thermal power $[W]$

ϵ Emissivity

σ Stefan-Boltzmann constant $[5.67 \cdot 10^{-8} W/m^2 K^4]$

A Area of battery surface $[m^2]$

C Nominal capacity $[Ah]$

C_p Mean heat capacity at constant pressure $[J/gK]$

E_{acc} Total dispersed energy $[J]$

E_d Dispersed energy $[J]$

E_{in} Initial energy $[J]$

h Convection heat transfer coefficient $[W/m^2 K]$

I Charge/Discharge current $[A]$

m Cell mass $[g]$

T Temperature $[K]$

t Time $[s]$

T^* Dimensionless temperature

U_{OC} Open circuit potential $[V]$

V Cell potential $[V]$

V_{max} Maximum cell potential $[V]$

1 Introduction

Currently, sustainable mobility is a crucial topic in a wide range of energy–saving and emission reduction scenarios. In this context, the development

and commercialisation of electric vehicles (EVs) is essential in minimising the environmental impact in our daily life [1, 2]. EVs commonly adopt lithium–ion (Li–ion) batteries as a power supply because of their higher energy density and specific power, lighter weight, lower self-discharge rates, higher recyclability, and longer cycle life than other rechargeable batteries [3–6].

This technology has been widely improved during the years from an electro-chemical point of view; however, thermal management of Li–ion batteries is still an open challenge. They are inherently subject to ageing not only over time but also due to operating conditions, including their state of charge (SOC), delivered/received current, and extreme operating temperatures. Temperature also has a certain influence on the performance degradation and lifetime of nearly all Li–ion cells when they are not operating in an appropriate temperature range (20°C – 40°C) [7, 8]. This is a crucial topic because several studies are devoted to the battery thermal management system (BTMS). In the existing studies, different cooling strategies have been proposed. The simplest method consists of air cooling systems, both in natural and forced convection, and is often supported by heat sinks/pin–fins [9, 10]. Liquid cooling strategies are more effective for EV applications because of their high thermal capacities. This technology exploits a single–phase or two–phase refrigerant [11–13], even with nano–fluid usage [14] that flows into a heat exchanger rounding the cells of the power module. In this configuration, despite its effectiveness, further thermal resistance is added owing to the presence of the heat exchanger. Moreover, in recent studies, the capability of innovative BTMS in controlling the thermal conditions of the power module, such as phase change materials [15, 16], heat pipes [17, 18], and pulsating heat pipes [19], have been investigated.

In this scenario, it is very important to evaluate battery heat generation. An appropriate determination of single–cell heat generation improves the BTMS design method. In a battery cell, heat generation is related to the following mechanisms: activation of interfacial kinetics, concentration species transport, and ohmic Joule heating from the movement of charged particles, which becomes significant for large cell sizes [20]. In the existing studies, battery heat generation has been separated into two main contributions: irreversible heat and reversible heat generation. The first term results from ohmic losses over the cell internal resistance, charge transfer overpotentials at the interface, and mass transfer limitations in the cell components. The second term is related to the entropic heat coefficient (EHC) which depends on the nature of the chemical reaction in the cell and the electrodes composition. In some previous studies, this reversible heat was neglected [21, 22] or considered constant with the SOC of the battery [23–25]. However, the entropic term can have a substantial influence on heat generation. Moreover, it could have a value of the same magnitude of irreversible heat [26, 27]. Consequently, the battery surface temperature simulation is also significantly influenced by the correct evaluation of the reversible heat [28]. The most common method of measuring the EHC is the potentiometric test [26, 27, 29–31]. Thomas et al. [30] emphasised that it is more effective to vary the temperature at a specific SOC. Nieto et al. [26] stated

3

that the EHC is not influenced by the temperature chosen for the thermal cycle and if it is evaluated during charge or discharge. The low influence of different thermal cycles was also observed by Madani et al. [31].

This study aims to apply IR thermography to quantitatively evaluate the heat generation of a cylindrical LiFePO$_4$ battery. Presently, some papers related to IR thermography of Li–ion cells have been published. In particular, pouch or prismatic cells have been mainly studied [32–38]. Kim et al. [32] used IR thermography to evaluate the surface temperature of a pouch cell to validate the numerical model presented. Menale et al. [33] also applied this technique to evaluate the temperature distribution on the battery surface for different battery types and discharge conditions. They also used these data to qualitatively study the effects of battery ageing. Goutam et al. [34] used infrared thermography to detect the location of the hottest region for the large pouch and prismatic cells of different geometries and materials. Robinson et al. [35] applied lock–in thermography to investigate the effect of periodic electro–thermal stimulation on both new and aged Li–ion pouch cells. Rani et al. [36] measured the surface temperature of the battery using thermocouples and IR thermography. The two methods were compared considering the temperature behaviour during discharge and the maximum value. Bazinski et al. [37] applied IR thermography to quantitatively evaluate the thermal power generation of a large pouch cell. Wang et al. [38] studied the thermal behaviour of a Li–ion through IR thermography. The IR images were used to evaluate the temperature fluctuation and distribution by analysing the variance and a local overheating index proposed by the authors.

Other studies have applied this technique to cylindrical batteries [29, 39–41]. Forgez et al. [29] developed a lumped parameter thermal model to estimate the internal temperature by measuring the surface temperature using thermocouples. In this study, IR thermography was used to verify the uniformity of the surface temperature. Robinson et al. [39] combined thermal imaging, X–ray tomography, and electrochemical impedance spectroscopy to study the thermal characteristics of a commercial cylindrical battery. IR thermography was used to characterise the heterogeneous temperature distributions during discharge. Chiew et al. [40] presented a pseudo–three–dimensional electrochemical–thermal model of a Li–ion cylindrical battery. Experimental measurements were performed with both thermocouples and IR thermography to validate the numerical model considering the battery surface temperature distribution. Wang et al. [41] proposed a thermal inertia prediction model for a cylindrical battery validated using IR thermography measurements.

Most of the reviewed papers applied infrared thermography to measure the surface temperature distribution. In this study, we used the experimental data in a simplified thermal model to estimate the thermal power generated. In our opinion, IR thermography can be considered a powerful method to evaluate battery heat generation with the advantage of being a fast and a non–intrusive measurement technique. To evaluate the reliability of IR thermography, our results were compared with thermocouple probe measurements. Furthermore,

electrical characterisation of the Li–ion battery was performed under a wide range of operating currents, and the cell potential during discharge, open circuit potential, and EHC were measured. These experimental data were used to calculate the battery heat generation using a simplified equation. Both irreversible and reversible heat terms were measured to carefully evaluate their contributions to the total heat generation.

The remainder of this paper is organised as follows. Section 2 introduces the heat generation term equation. The experimental setup is described in Section 3. Section 4 presents the results. Section 5 is devoted to the evaluation of the battery heat generation. Finally, the conclusions are presented in Section 6.

2 Heat generation model

Bernardi et al. [42] proposed a complete thermodynamic energy balance for Li–ion batteries. The energy balance can be expressed using Eq. (1). The energy accumulation in the cell is equal to the heat generated minus the heat loss through convection and radiation.

$$mC_p\frac{dT}{dt} = \dot{Q} - hA(T_s - T_e) - \epsilon\sigma A(T_s^4 - T_e^4) \tag{1}$$

In present studies, a simplified equation, derived from Bernardi et al., is commonly adopted to evaluate heat generation in Li–ion batteries [20, 22, 26, 27, 29, 30, 43]:

$$\dot{Q} = \underbrace{I \cdot (V - U_{OC})}_{\dot{Q}_{irr}} + \underbrace{I \cdot T \cdot \frac{\partial U_{OC}}{\partial T}}_{\dot{Q}_{rev}} \tag{2}$$

where I is the discharge current, V is the battery potential, T is the battery temperature (expressed in K), U_{OC} is the open circuit potential, and $\partial U_{OC}/\partial T$ is the EHC.

The irreversible term of the equation depends on the cell overpotential, which is equal to the difference between V and U_{OC} and the operating current. This is indicative of all irreversible processes such as Joule heating within the battery owing to internal resistance and the energy dissipated in electrode overpotentials. In this study, the operating current was fixed to be negative during discharge. This implies that the irreversible contribution is always positive.

The reversible term in Eq. (2) is related to the entropy change in the electrochemical reaction and is strongly influenced by the EHC. This coefficient varies significantly with the SOC and chemistry of the battery. It can be negative or positive; a negative value means that reversible heat is exothermic, whereas a positive value of EHC signifies that reversible heat is endothermic during the discharge process.

5

Eq. (2) allows evaluates the thermal power generated during the battery discharge. We can also determine the instantaneous energy dispersed in the form of heat generation:

$$E_d = \dot{Q} \cdot \Delta t \tag{3}$$

where Δt is the time interval at which the heat was generated. The total amount of dispersed energy can be expressed using Eq. (4), where τ is the time required to fully discharge the battery at the operating current.

$$E_{acc} = \int_0^\tau E_d \, dt \tag{4}$$

Finally, the battery efficiency could be defined as follows:

$$\eta = \frac{E_{in} - E_{acc}}{E_{in}} \tag{5}$$

where E_{in} is the initial battery energy assumed to be equal to the maximum electric energy that the battery can supply without any losses. Therefore, the numerator in Eq. (5) is the electric energy supplied by the battery. The ideal electric energy is defined using Eq. (6), where V_{max} is the battery voltage when fully charged, and C is the nominal capacity of the cell.

$$E_{in} = V_{max} \cdot C \tag{6}$$

In the above equations, the variables E_{in}, E_{acc}, and E_d are expressed in Joule.

3 Experimental apparatus

In this study, the thermal behaviour of a commercial LiFePO$_4$ battery was determined during the discharge process. The battery used in the experiments was A123 26650 (series name ANR26650M1–B). It is a cylindrical cell of diameter 26 mm, height 65 mm, and weight 76 g. The nominal battery voltage was 3.3 V and the maximum voltage when fully charged was 3.6 V. The cell capacity was 2.5 Ah with a maximum continuous discharge current of 70 A. The active materials of the positive and negative electrodes were LiFePO$_4$ and LiC$_6$, respectively, and the electrolyte was LiPF$_6$ dissolved in a mixture of 2:1 ethylene carbonate/dimethyl carbonate. The current collectors were made of aluminium and copper.

The cell charge and discharge processes are managed by a programmable power supply (RMX–4125) and DC electronic load (RMX–4005) controlled through a LabVIEW routine. The current setting accuracy of the electronic load was $\pm0.1\%$ F.S. ranging from 0 to 70 A with a resolution of 2 mA. The current and voltage of the battery were constantly measured during the entire process. The

voltage was directly measured using an NI 6289 data acquisition device with a resolution of $0.076 \ mV$ ranging from 0 to $10 \ V$ and uncertainty of $\pm 0.25 \ mV$. The operating current was measured using a current transducer with an uncertainty of $\pm 0.02 \ A$ in the range $\pm 85 \ A$. Ambient parameters (temperature and relative humidity) were measured with an uncertainty of ± 0.6°C and $\pm 2.5\%$ for temperature and relative humidity, respectively. Transducer signals of the current and ambient parameters were then acquired using the NI 6289 data acquisition device.

Battery surface temperature measurements were performed using thermocouples and IR thermography. Four T–type thermocouples were placed along the height of the battery with a high–conductivity adhesive. The thermocouples were attached to an ice point reference before being acquired by the data logger. They were previously calibrated by submerging the battery into a high–precision calibration bath. This procedure allows us to obtain an uncertainty of ± 0.05°C. Thermographic measurements were performed using a FLIR SC3000 IR camera equipped with a 320 x 240 QWIP sensor array and a 20° lens with a 20° x 15° field of view with a minimum focus distance of $0.3 \ m$. The thermal sensitivity was $20 \ mK$ at 30°C, with an uncertainty of $\pm 1\%$ of the measured value. The battery was covered with black matte paint with an emissivity of 0.94, measured through a black body.

Fig. 1 shows the measurement setup described above and the thermocouple arrangement on the battery surface.

During the tests, we performed the following measures: battery voltage, operating current, and temperature (using thermocouples) which were continuously recorded at $10 \ Hz$. Meanwhile, IR images were also acquired once per second. The thermal camera was placed at a distance of $0.3 \ m$ from the battery, resulting in a spatial resolution of $0.3 \ mm$ per pixel. Each image obtained during discharge was then subtracted from the reference thermal image related to the initial condition. In addition, thermocouple measurements are referred to as the initial value to avoid the influence of environmental temperature variation. The ambient temperature and relative humidity were measured during the tests. These values were used in the thermographic image acquisition software as input parameters to perform temperature measurements. The ambient temperature for all tests was between 21°C and 23°C. Thermal images were processed using MATLAB. Four areas of 10 x 10 pixels were selected in the same position of the four thermocouples along the battery height and in the middle line of the battery width. The extension of these areas was chosen by analysing the ratio between the view factor of the cylindrical surface and that of a flat plate. In the reference areas, the ratio assumes a minimum value of 0.987; consequently, the error introduced by the view factor was considered negligible in these areas. The mean temperature was calculated in the reference areas to compare the two measurement methods.

Uncertainty analysis was performed according to the reference regulation. In this study, we considered the instrument uncertainty for the parameters directly acquired (i.e. thermocouples, cell potential, and current). Type A

uncertainty was considered in the case of mean values (i.e. U_{OC} and EHC). For correlated quantities (i.e. thermal power generated and total dispersed energy), the combined uncertainties were evaluated. Finally, a coverage factor of 2 was considered in the calculation of the expanded uncertainties. The obtained uncertainties are ± 0.25 mV for U_{OC} measurements and 0.3% for the SOC calculation. This last value is due to the setting current accuracy of the electronic load and the measurement uncertainty of the current sensor. In the evaluation of the EHC, we obtained an uncertainty of ± 0.001 mV/K. The measurement uncertainty of the correlated quantities is summarised in Table 1, where the largest percentage uncertainty for each C–rate is reported. The C–rate is the rate at which a battery is charged or discharged. It is defined as the ratio between the discharge current applied and the discharge current under which the battery delivers its nominal capacity per hour.

4 Experimental results

Eq. (2) requires several parameters to be determined to evaluate the battery heat generation. In this study, three types of tests were performed to experimentally determine these quantities. U_{OC} and EHC were evaluated every 10% of the SOC from full charge to complete discharge. The first with subsequent cycles of discharge and relaxation, and the second through a potentiometric test. Finally, a constant current discharge was applied to the battery to measure the cell potential, operating current, and surface temperature.

4.1 Open circuit potential

The open circuit potential was evaluated at every 10% of the SOC using the method described below. First, the battery was discharged at a specific SOC by a low operating current of 2.5 A. It was then allowed to relax for 1 h. At the end of the relaxation, the voltage value reached by the battery is the U_{OC} at a particular SOC. This test was repeated 5 times, and the U_{OC} value used in Eq. (2) is the mean value of the 5 tests; it is also shown in the plots in Fig. (2). The maximum percentage difference between each test and the mean value was very low (0.07%). This ensured the excellent repeatability of the measurements.

8

4.2 Entropic Heat Coefficient

The battery was discharged to a specific SOC with a discharge current of 2.5 A and was allowed to relax. The relaxation was followed by a thermal cycle in a thermostatic bath with a setting accuracy of ± 0.5°C. The open circuit potential of the battery was constantly measured during the bath temperature variation. The thermal cycle used in this study consisted of 3 h at 25°C, 3 h at 10°C, 3 h at 35°C, 3 h at 45°C, and 3 h at 25°C. Temperature values were chosen in the range where the battery operates safely (as recommended in the datasheet). This procedure was repeated every 10% of SOC until complete discharge. Fig. 3 shows an example of the open circuit potential variation during the thermal cycle. The voltage values measured in the last 15 min of each temperature step were considered U_{OC} steady-state values. The mean values of this temporal window are plotted as a function of temperature, as shown in Fig. 4. The gradient of the curve determines the EHC for each SOC. Finally, Fig. 5 shows the EHC measured as a function of SOC. The EHC assumes positive values until an SOC of 30%; subsequently, it becomes negative. Similar behaviour was also observed in previous studies [29, 43]. Therefore, the reversible heat would be negative; thus, its effect is endothermic during the discharge process until 30% of SOC. Successively, as discharge proceeds, the reversible heat change its behaviour and it exhibits an exothermic effect, and it starts to assume positive values.

4.3 Constant current discharge

In this test, the battery was fully discharged with a constant operating current. The discharge was stopped when the cell potential reached a minimum voltage of 2 V. The test was performed at ambient temperature and under a wide range of C–rates (Table 2). After the complete discharge, the battery is fully re–charged with a constant current constant voltage procedure: first, a constant current of 1 C was applied until the battery reaches the maximum voltage of 3.6 V (CC phase); subsequently, the voltage was kept constant until the operating current decreases to 25 mA (CV phase).

The cell potential at different discharge rates is reported as a function of the SOC in Fig. 6. When a current is required from the battery, the cell potential has a sudden fall owing to its internal resistance, and it flattens until a very low SOC when the voltage falls to its minimum value. For a higher discharge current, the voltage value of the flattened zone always decreases, and the difference with the open circuit potential rapidly increases. When the cell potential decreases, the surface temperature of the battery increases, especially at low SOC. The temperature rise results from the loss of the initial energy as heat generated by the battery. Fig. 7 shows the thermal images acquired for

9

the discharge rates tested. For each discharge rate, 4 SOC levels were chosen as representative points for the discharge: 75%, 50%, 25%, and 0%. The images show the difference between the temperature value measured during discharge and its initial value (before the test starts). The ambient temperature, relative humidity, and distance from the battery surface were considered in the infrared image acquisitions. The colour scale applied to the images was always the same for the tests to appreciate the temperature increase with the C–rate. Thermal images underline the warm–up of the battery during discharge. It is clear that a higher current produces a higher temperature rise. The temperature reached by the battery at the end of discharge is moderate for lower C–rates (approximately 10°C greater ambient temperature) but becomes very high when higher C–rates occur. In these cases, the battery far exceeds its operating temperature range. For a discharge current of 10 C, the final temperature was 45°C higher than the initial temperature. Furthermore, for all C–rates, the battery surface temperature was not uniform across its height; however, there was a greater temperature in the upper zone at the negative electrode. This trend is also confirmed using thermocouple measurements, as shown in Fig. 8, where only a case of 2 C is reported for compactness. This effect can be attributed to natural convection on the battery surface. On the bottom side, there is a higher heat transfer, while proceeding upwards, the surrounding air is influenced by the surface temperature and the heat transfer decreases.

Finally, Fig. 9 shows the temperature trend measured by the thermocouples and IR thermography for all the discharge currents tested. The IR thermography results, illustrated in Fig. 9, were obtained from an averaging procedure involving the four reference areas described in Section 3.

Fig. 9 shows that the temperature rises with greater intensity at a low SOC when the voltage sharply decreases. Furthermore, IR thermography perfectly copies the thermocouple data and the temperature trend is in good agreement. We also introduced a percentage difference between the mean temperatures measured by thermocouples and IR thermography, expressed using Eq. (7):

$$\delta = 100 \cdot \left| \frac{T_{tc} - T_{IR}}{(T_{eod} - T_{in})_{tc}} \right| \tag{7}$$

where the subscript "tc" refers to thermocouple data and "IR" to thermography. T_{eod} is the temperature at the end of discharge, and T_{in} is the initial value. This parameter was calculated for each acquisition during the discharge; however, in Table 3, only the maximum value of δ for each C–rate was reported for compactness. The maximum absolute temperature difference recorded between the two measurement methods is also reported in Table 3.

This analysis confirmed that the IR thermography temperature values were close to the thermocouple measurements. The absolute temperature difference is always less than 1°C. The parameter δ shows the error of IR thermography compared to the range of temperature measured during discharge. The higher values correspond to a low C–rate, where the increase in surface temperature

10

is small.

5 Determination of the heat generated

Once the open circuit potential and EHC were measured, the thermal power generated can be determined using Eq. (2) for all constant–current discharges. In Eq. (2), we use the surface temperature measured using thermocouples and infrared thermography. We considered a uniform temperature inside the battery because the Biot number assumes a value lower than 0.1; this could be a good approximation for a low C–rate, whereas, for a high discharge current, the error in the absolute thermal power value can be larger. This measurement error was estimated by considering the temperature difference between the surface and the internal part of the battery at 15°C experimentally measured by Forgez et al. for a discharge current of 20 A [29]. Thermal power was also evaluated with this increased temperature, and a maximum percentage difference of 1% was found.

Fig. 10 shows the instantaneous thermal power at each SOC and the accumulated heat through the discharge process for all C–rates tested. Because the overpotential increases with the discharge current, the thermal power and accumulated heat are also greater at higher C–rates. Furthermore, thermal power has a faster increase at low SOC, where the battery voltage has an abrupt decay and the EHC becomes negative. In this zone, the reversible thermal power is positive, and it increases the generated total thermal power. Otherwise, when EHC reaches its maximum positive value (approximately SOC equal to 60%), the thermal power shows a minimum for all discharge currents. From the above considerations, it can be understood that the thermal power generated by the battery is significantly influenced by the reversible part. The heat accumulated during all discharges was compared to the initial energy available to obtain the battery efficiency, as expressed in Eq. (5). Table 4 shows the efficiency for all discharge currents and the electric power supply by the battery. Similarly, it can be noticed that at higher discharge currents, the efficiency decreases owing to the greater overpotential and increase in the battery temperature. The battery supplies a greater electric power at higher C–rates; however, the efficiency is low, owing to the increase in thermal power generated.

The two contributions of the total thermal power generated were analysed individually. Fig. 11 shows Q_{irr}/Q_{tot} and Q_{rev}/Q_{tot} as functions of SOC at C–rates of 0.5 C, 2 C, 5 C, and 10 C.

The reversible heat considerably influences the total heat generated by the battery, especially at low C–rates, where it has the same order of magnitude as the irreversible heat. It can also be seen that when the EHC is positive, the reversible heat is negative, and the discharge process is endothermic. In

11

this case, the reversible part was subtracted from the total heat generation. Otherwise, from an SOC of 20%, the EHC becomes negative, the discharge process is exothermic, and the reversible component increases the total thermal power generation. As shown in Fig. 11, if only the irreversible part of heat generation is considered, the total heat would be widely overestimated at low C–rates. The error in the heat evaluation became less significant at higher C–rates. In these cases, the reversible term can be considered negligible because its value is much lower than the irreversible thermal power. Furthermore, it is assumed that a constant value of EHC is not a suitable choice because the contribution of the reversible term to the total heat is significantly influenced by the SOC.

However, at higher discharge rates, the reversible contribution is always less significant. At higher C–rates, the overpotential is very large, and the irreversible term in Eq. (2) becomes predominant. The increase in overpotential with the C–rate resulted from the ohmic loss on the internal resistance of the battery.

The reversible term also influenced the surface distribution of the battery temperature during the discharge process. This is seen in Fig. 12, where a dimensionless temperature is shown for all C–rates as a function of the SOC. The dimensionless temperature is defined using Eq. (8):

$$T^* = \frac{T - T_{in}}{T_{eod} - T_{in}} \tag{8}$$

Fig. 12 shows that T^* assumes an almost linear trend for a current of 10 C where the overpotential has a very large value. Here, the reversible term in Eq. (2) assumes a very low value when compared with the irreversible term, and the thermal power is mostly influenced by these components. When the discharge current is decreased, this linearity is always less significant because the EHC becomes relevant with respect to the overpotential. Furthermore, all the lines have a unique point of intersection (except for 0.5C) at approximately 60% of the SOC when the EHC reaches its maximum value. After this point, the temperature is higher for higher C–rates, as shown in Fig. 9; conversely, before the intersection point, the trend is almost the opposite. This is an interesting result obtained from the dimensionless temperature plot; however, further tests on different battery models and chemistry compositions should be performed to confirm this behaviour.

Finally, the aforementioned estimations were also applied to the IR thermography data. From Table 3, it can be observed that the thermography and thermocouple data are comparable. This evidence also produces a similar prediction of the reversible heat and total thermal power. The error made by thermography on reversible heat calculation is approximately 0.3%, whereas that of the thermal power is less than 0.1% for all discharge currents, as shown in Table 5.

12

6   Conclusion

In this study, the thermal behaviour of a LiFePO$_4$ Li–ion battery under various discharge currents was experimentally investigated. Moreover, electrical characterisation of the cell was performed to obtain the open circuit potential and EHC. Heat generation was evaluated using a simplified equation that considers both irreversible and reversible contributions. The thermal power estimation was based on battery surface temperature measurements performed with thermocouples and IR thermography.

The results show an increase in the thermal power when the battery is subjected to higher discharge currents. This is due to the increase in overpotential, which is related to a greater battery voltage drop. Consequently, the battery efficiency decreased with higher C–rates. At low SOC, the greatest thermal power was observed because of the abrupt decay of voltage and the negative value of EHC. This also leads to a sharp increase in temperature which reaches very high values over the maximum recommended operating temperature. The contribution of the reversible and irreversible heat to the total thermal power was carefully evaluated. The reversible part cannot be assumed to be constant or not considered at all, because it significantly influences the total thermal power and temperature trend, especially at low C–rates. IR thermography and thermocouple probe measurements showed that the surface temperature was not uniform along the height of the battery. There was a greater warm–up in the upper zone. The temperature measurements performed with IR thermography were in good agreement with the thermocouple results. It has been shown that the temperature trend during discharge is the same for both methods. Furthermore, the maximum deviation of thermography data from the thermocouples is always less than 1°C. These differences lead to an error of less than 0.1% in thermal power evaluation.

The obtained results show that IR thermography allows an excellent estimation of thermal power with values very close to the thermocouple data. Moreover, IR approaches can quickly scan the measurement area and are non–intrusive methods of analysis. In contrast, thermocouples must be placed on the battery surface with a special highly conductive adhesive, and they have a more complex acquisition system. Therefore, in our opinion, IR thermography can be considered a powerful method, not only to qualitatively evaluate thermal behaviour but to also perform a quantitative assessment of the heat generated by the Li–ion battery.

References

[1] M. Wada, Research and development of electric vehicles for clean transportation, Journal of Environmental Sciences 21 (6) (2009) 745–749.

13

[2] H. de Wilde, P. Kroon, Policy options to reduce passenger cars CO2 emissions after 2020, ECN ECN-E–13-005.

[3] M. Lowe, S. Tokuoka, T. Trigg, G. Gereffi, Lithium-ion batteries for electric vehicles: the u.s. value chain, Duke University Center on Globalization, Governance and Competitiveness, Tech. Rep.

[4] E. Karden, S. Ploumen, B. Fricke, T. Miller, K. Snyder, Energy storage devices for future hybrid electric vehicles, Journal of Power Sources 168 (1) (2007) 2–11.

[5] T. Mller, Lithium ion battery automotive applications and requirements, in: Seventeenth Annual Battery Conference on Applications and Advances. Proceedings of Conference (Cat. No.02TH8576), 2002, pp. 113–118.

[6] J. Speirs, M. Contestabile, Y. Houari, R. Gross, The future of lithium availability for electric vehicle batteries, Renewable and Sustainable Energy Reviews 35 (2014) 183–193.

[7] H. Mettlach, R. Matthe, L. Turner, Voltec battery system for electric vehicle with extended range, SAE International Journal of Engines 4 (1) (2011) 1944–1962.

[8] A. Pesaran, S. Santhanagopalan, G. Kim, Addressing the impact of temperature extremes on large format li-ion batteries for vehicle applications (presentation), Tech. rep., National Renewable Energy Lab.(NREL), Golden, CO (United States) (2013).

[9] P. Qin, M. Liao, W. Mei, J. Sun, Q. Wang, The experimental and numerical investigation on a hybrid battery thermal management system based on forced-air convection and internal finned structure, Applied Thermal Engineering 195 (2021) 117212.

[10] S. K. Mohammadian, Y. Zhang, Thermal management optimization of an air-cooled li-ion battery module using pin-fin heat sinks for hybrid electric vehicles, Journal of Power Sources 273 (2015) 431–439.

[11] H. Wang, T. Tao, J. Xu, X. Mei, X. Liu, P. Gou, Cooling capacity of a novel modular liquid-cooled battery thermal management system for cylindrical lithium ion batteries, Applied Thermal Engineering 178 (2020) 115591.

[12] Y. Fang, F. Ye, Y. Zhu, K. Li, J. Shen, L. Su, Experimental investigation on system performances and transient response of a pumped two-phase battery cooling system using r1233zd, Energy Reports 6 (2020) 238–247.

[13] J. Duan, J. Zhao, X. Li, S. Panchal, J. Yuan, R. Fraser, M. Fowler, Modeling and analysis of heat dissipation for liquid cooling lithium-ion batteries, Energies 14 (14) (2021) 4187.

[14] S. Wiriyasart, C. Hommalee, S. Sirikasemsuk, R. Prurapark, P. Naphon, Thermal management system with nanofluids for electric vehicle battery cooling modules, Case Studies in Thermal Engineering 18 (2020) 100583.

[15] X. Duan, G. Naterer, Heat transfer in phase change materials for thermal management of electric vehicle battery modules, International Journal of Heat and Mass Transfer 53 (23) (2010) 5176–5182.

[16] Y. Li, Y. Du, T. Xu, H. Wu, X. Zhou, Z. Ling, Z. Zhang, Optimization of thermal management system for li-ion batteries using phase change material, Applied Thermal Engineering 131 (2018) 766–778.

[17] N. Putra, A. F. Sandi, B. Ariantara, N. Abdullah, T. M. Indra Mahlia, Performance of beeswax phase change material (pcm) and heat pipe as passive battery cooling system for electric vehicles, Case Studies in Thermal Engineering 21 (2020) 100655.

[18] Y. Gan, L. He, J. Liang, M. Tan, T. Xiong, Y. Li, A numerical study on the performance of a thermal management system for a battery pack with cylindrical cells based on heat pipes, Applied Thermal Engineering 179 (2020) 115740.

[19] M. Chen, J. Li, Nanofluid-based pulsating heat pipe for thermal management of lithium-ion batteries for electric vehicles, Journal of Energy Storage 32 (2020) 101715.

[20] T. M. Bandhauer, S. Garimella, T. F. Fuller, A critical review of thermal issues in lithium-ion batteries, The Electrochemical Society 158 (3) (2011) R1.

[21] K. Smith, C.-Y. Wang, Power and thermal characterization of a lithium-ion battery pack for hybrid-electric vehicles, Journal of Power Sources 160 (1) (2006) 662–673.

[22] C. R. Pals, J. Newman, Thermal modeling of the lithium/polymer battery: II . temperature profiles in a cell stack, The Electrochemical Society 142 (10) (1995) 3282–3288.

[23] Y. Chen, J. W. Evans, Heat transfer phenomena in lithium/polymer-electrolyte batteries for electric vehicle application, The Electrochemical Society 140 (7) (1993) 1833–1838.

[24] S.-C. Chen, Y.-Y. Wang, C.-C. Wan, Thermal analysis of spirally wound lithium batteries, The Electrochemical Society 153 (4) (2006) A637.

[25] Y. Chen, J. W. Evans, Thermal analysis of lithium polymer electrolyte batteries by a two dimensional model-thermal behaviour and design optimization, Electrochimica Acta 39 (4) (1994) 517–526.

[26] N. Nieto, L. Díaz, J. Gastelurrutia, I. Alava, F. Blanco, J. C. Ramos, A. Rivas, Thermal modeling of large format lithium-ion cells, The Electrochemical Society 160 (2) (2012) A212–A217.

[27] B. Manikandan, C. Yap, P. Balaya, Towards understanding heat generation characteristics of li-ion batteries by calorimetry, impedance, and potentiometry studies, The Electrochemical Society 164 (12) (2017) A2794–A2800.

[28] M. Shadman Rad, D. Danilov, M. Baghalha, M. Kazemeini, P. Notten, Adaptive thermal modeling of li-ion batteries, Electrochimica Acta 102 (2013) 183–195.

[29] C. Forgez, D. Vinh Do, G. Friedrich, M. Morcrette, C. Delacourt, Thermal modeling of a cylindrical lifepo4/graphite lithium-ion battery, Journal of Power Sources 195 (9) (2010) 2961–2968.

15

[30] K. E. Thomas, C. Bogatu, J. Newman, Measurement of the entropy of reaction as a function of state of charge in doped and undoped lithium manganese oxide, The Electrochemical Society 148 (6) (2001) A570.

[31] S. S. Madani, E. Schaltz, S. Knudsen Kær, An experimental analysis of entropic coefficient of a lithium titanate oxide battery, Energies 12 (14) (2019) 2685.

[32] U. S. Kim, C. B. Shin, C.-S. Kim, Effect of electrode configuration on the thermal behavior of a lithium-polymer battery, Journal of Power Sources 180 (2) (2008) 909–916.

[33] C. Menale, F. D'Annibale, B. Mazzarotta, R. Bubbico, Thermal management of lithium-ion batteries: An experimental investigation, Energy 182 (2019) 57–71.

[34] S. Goutam, J.-M. Timmermans, N. Omar, P. V. d. Bossche, J. Van Mierlo, Comparative study of surface temperature behavior of commercial li-ion pouch cells of different chemistries and capacities by infrared thermography, Energies 8 (8) (2015) 8175–8192.

[35] J. B. Robinson, E. Engebretsen, D. P. Finegan, J. Darr, G. Hinds, P. R. Shearing, D. J. L. Brett, Detection of internal defects in lithium-ion batteries using lock-in thermography, The Electrochemical Society 4 (9) (2015) A106–A109.

[36] M. Rani, Z. Razlan, A. Shahriman, Z. Ibrahim, W. Wan, Comparative study of surface temperature of lithium-ion polymer cells at different discharging rates by infrared thermography and thermocouple, International Journal of Heat and Mass Transfer 153 (2020) 119595.

[37] S. Bazinski, X. Wang, Predicting heat generation in a lithium-ion pouch cell through thermography and the lumped capacitance model, Journal of Power Sources 305 (2016) 97–105.

[38] S. Wang, K. Li, Y. Tian, J. Wang, Y. Wu, S. Ji, Infrared imaging investigation of temperature fluctuation and spatial distribution for a large laminated lithium–ion power battery, Applied Thermal Engineering 152 (2019) 204–214.

[39] J. B. Robinson, J. A. Darr, D. S. Eastwood, G. Hinds, P. D. Lee, P. R. Shearing, O. O. Taiwo, D. J. Brett, Non-uniform temperature distribution in li-ion batteries during discharge – a combined thermal imaging, x-ray micro-tomography and electrochemical impedance approach, Journal of Power Sources 252 (2014) 51–57.

[40] J. Chiew, C. Chin, W. Toh, Z. Gao, J. Jia, C. Zhang, A pseudo three-dimensional electrochemical-thermal model of a cylindrical lifepo4/graphite battery, Applied Thermal Engineering 147 (2019) 450–463.

[41] S. Wang, K. Li, Y. Tian, J. Wang, Y. Wu, S. Ji, An experimental and numerical examination on the thermal inertia of a cylindrical lithium-ion power battery, Applied Thermal Engineering 154 (2019) 676–685.

[42] D. Bernardi, E. Pawlikowski, J. Newman, A general energy balance for battery systems, The Electrochemical Society 132 (1) (1985) 5–12.

16

[43] F. Geifes, C. Bolsinger, P. Mielcarek, K. P. Birke, Determination of the entropic heat coefficient in a simple electro-thermal lithium-ion cell model with pulse relaxation measurements and least squares algorithm, Journal of Power Sources 419 (2019) 148–154.
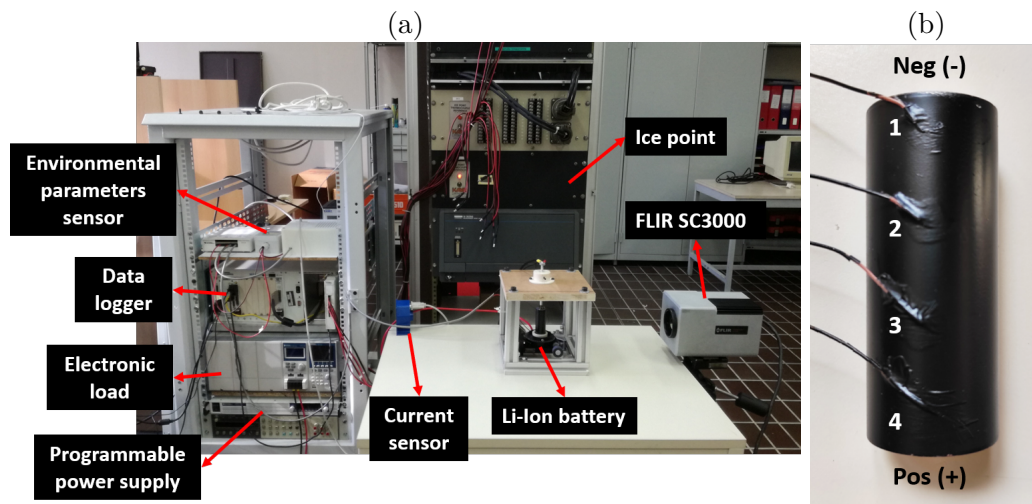
17

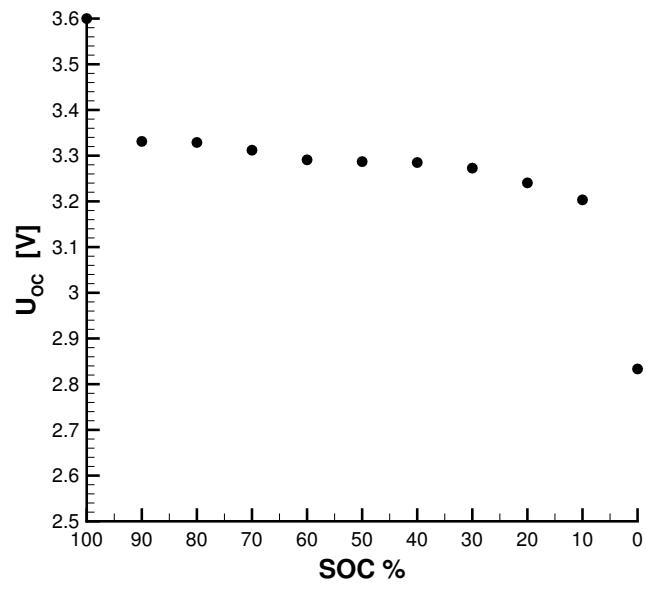Figure 1. Experimental setup (a) and thermocouples arrangement on battery surface (b).

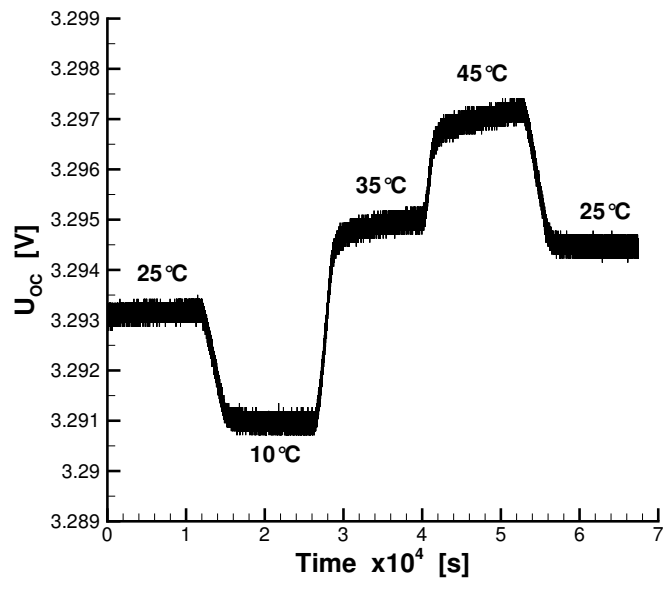Figure 2. Open circuit potential of the battery as a function of SOC.
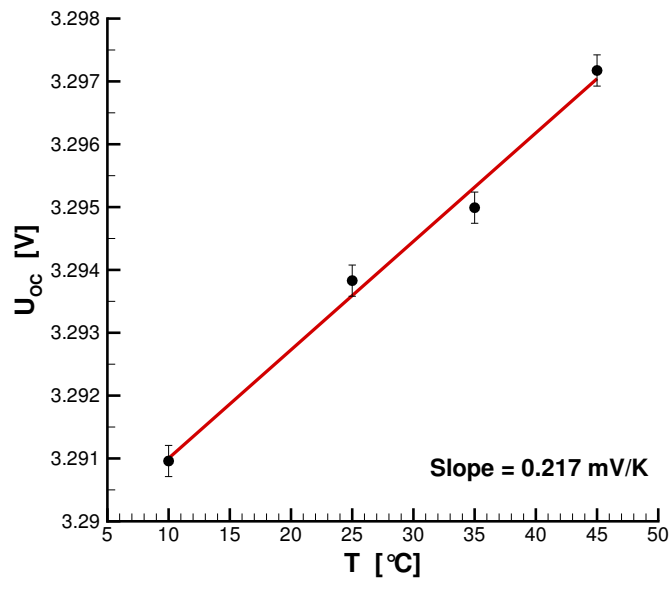
Figure 3. Open circuit potential measured during thermal cycle at SOC 50%.

Figure 4. U_{OC} as a function of temperature at SOC 50%.
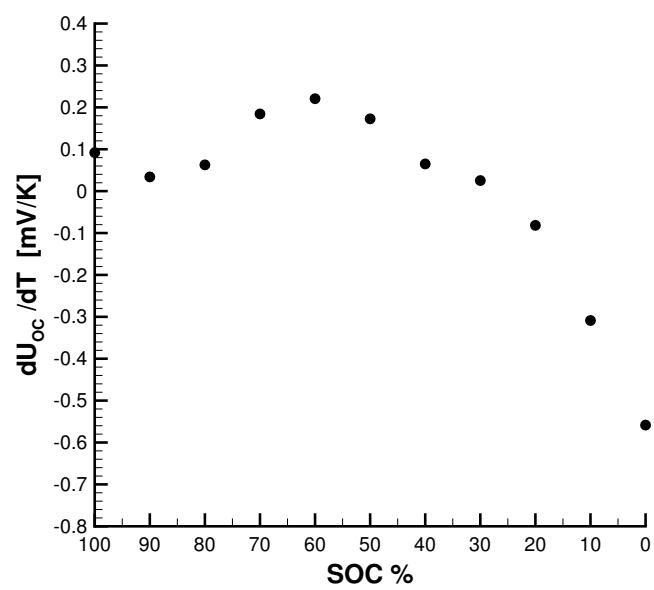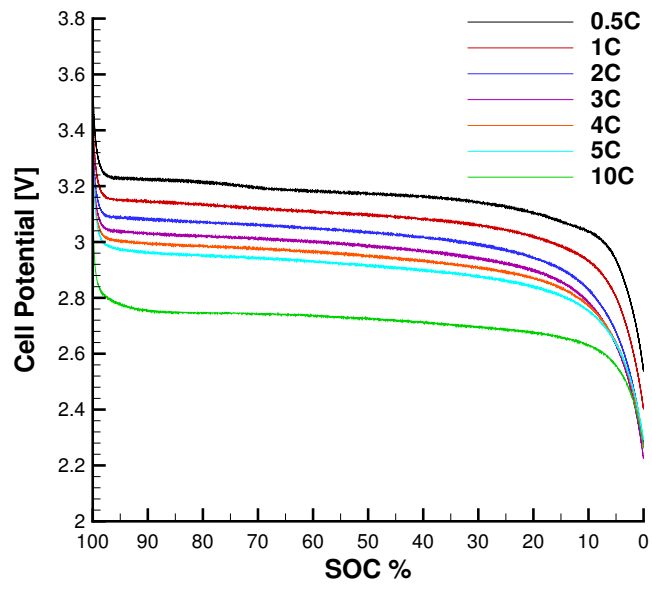
Figure 5. Entropic heat coefficient as a function of SOC.

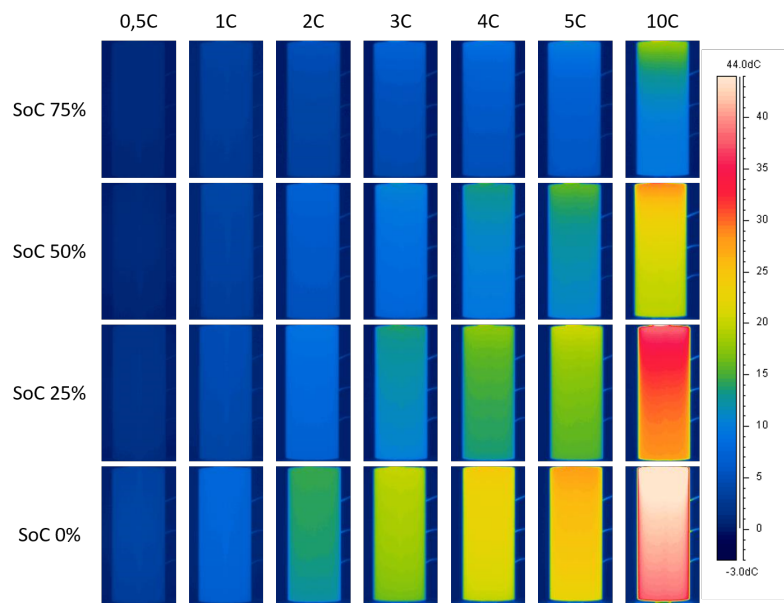Figure 6. Cell potential as a function of SOC for different C–rate.

Figure 7. Thermal images of the battery at various discharge rates and SOC levels.
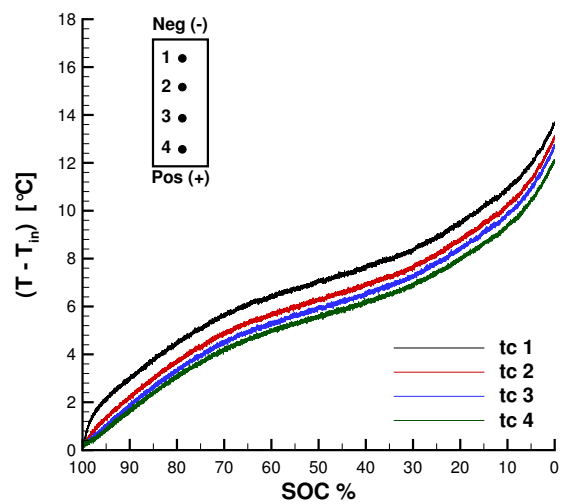
Figure 8. Temperature measured using the four thermocouples for a discharge current of 2 C.
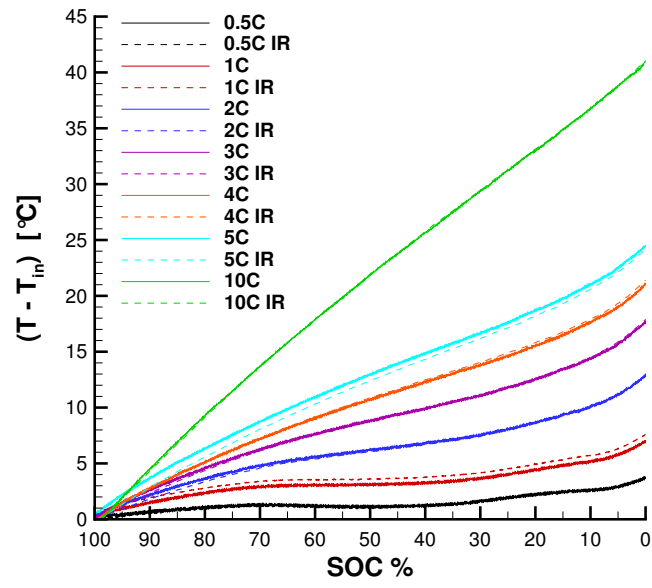
Figure 9. Battery surface temperature for different C–rate measured using thermo-couples (solid line) and IR thermography (dashed line).
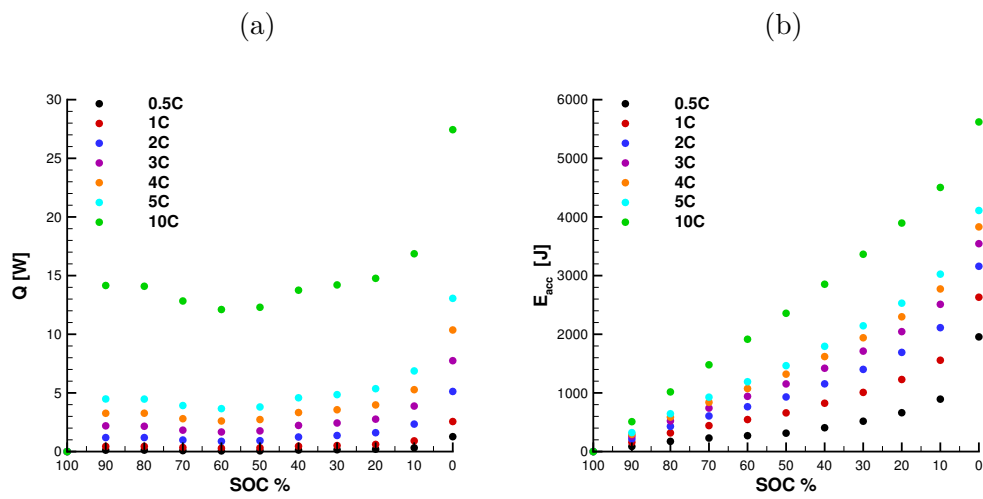
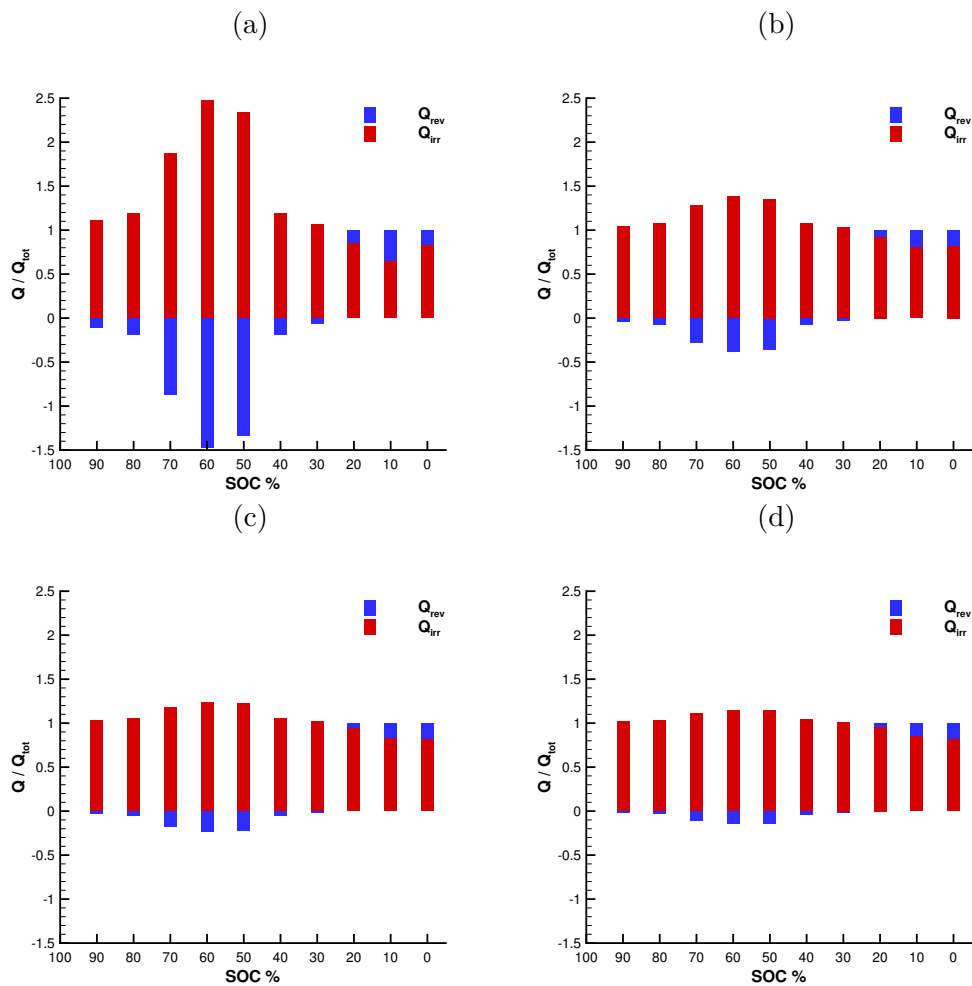Figure 10. Thermal power generated (a) and accumulated heat (b) at various discharge currents.

Figure 11. Contributions of the irreversible and reversible parts to the total thermal power generated as a function of SOC for a discharge current of 0.5 C (a), 2 C (b), 5 C (c), and 10 C (d).
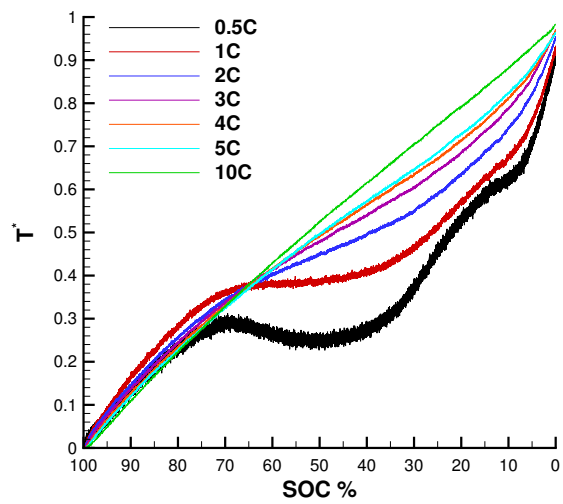
Figure 12. Dimensionless temperature for different C–rates.

Table 1
Measurement uncertainty.

C-rate	0.5	1	2	3	4	5	10
$\dot{Q}_{irr}\%$	± 0.69	± 0.37	± 0.24	± 0.19	± 0.16	± 0.14	± 0.079
$\dot{Q}_{rev}\%$	± 0.55	± 0.39	± 0.35	± 0.35	± 0.38	± 0.41	± 0.51
$\dot{Q}\%$	± 1.84	± 0.6	± 0.34	± 0.24	± 0.2	± 0.17	± 0.09
$E_{acc}\%$	± 1.7	± 0.71	± 0.45	± 0.34	± 0.28	± 0.25	± 0.14

Table 2
Constant current discharge tests performed.

C-rate	0.5	1	2	3	4	5	10
Current [A]	1.25	2.5	5	7.5	10	12.5	25
Time [s]	7200	3600	1800	1200	900	720	360

Table 3
The absolute maximum difference between thermocouples and thermographic temperature measurements.

C-rate	0.5	1	2	3	4	5	10
ΔT $[^{\circ}C]$	0.25	0.74	0.47	0.38	0.46	0.88	0.3
δ %	6.51	10.28	3.57	2.1	2.1	3.58	0.72

Table 4
Battery efficiency.

C-rate	0.5	1	2	3	4	5	10
η	0.94	0.92	0.9	0.89	0.88	0.87	0.82
Q_{el} [W]	4.23	8.27	16.24	20.05	31.74	39.29	74.38

Table 5
Maximum percentage difference between IR thermography and thermocouples on heat calculations.

C-rate	0.5	1	2	3	4	5	10
$\dot{Q}\%$	0.075	0.047	0.062	0.034	0.068	0.071	0.083
$\dot{Q}_{rev}\%$	0.09	0.12	0.15	0.1	0.19	0.23	0.34